

Crystal Structure, Band Structure, and Physical Properties of $\text{Ba}_8\text{Cu}_{6-x}\text{Ge}_{40+x}$ ($0 \leq x \leq 0.7$)

Simon Johnsen, Anders Bentien, Georg K. H. Madsen, and Bo B. Iversen*

Department of Chemistry, University of Aarhus, Aarhus, Denmark

Mats Nygren

Department of Inorganic Chemistry, University of Stockholm, Stockholm, Sweden

Received May 22, 2006. Revised Manuscript Received July 11, 2006

Eight samples with nominal stoichiometry $\text{Ba}_8\text{Cu}_{6-x}\text{Ge}_{40+x}$, $x = 0-0.7$, have been synthesized with a new method involving $\text{Ba}_6\text{Ge}_{25}$ as an intermediate step. The new route provides fine control of the Cu:Ge ratio and allows systematic studies of the changes in the transport properties as a function of x . Resistivity, thermopower, and Hall carrier concentration all show systematic changes upon altering the Cu:Ge ratio. On the basis of density functional theory, we have calculated the electrical transport properties for fully ordered $\text{Ba}_8\text{Cu}_6\text{Ge}_{40}$. An optimal power factor is predicted for a Fermi level in the top of the valence band. Contrary to expectation, n -type behavior is observed in all samples, which appears to be due to small amounts of vacancies. Relatively low mobilities result in moderate thermoelectric properties with $ZT = 0.07$ at 400 K for the $x = 0.2$ sample.

Introduction

The design concepts used in thermoelectrics for many years were those originally proposed by Ioffe.¹ To ensure a high thermopower and a low thermal conductivity, he targeted semiconducting compounds composed of heavy elements. The best thermoelectric performance was achieved in doped binary compounds. More recently, another approach was proposed by Slack that spurred a search for so-called “phonon glasses and electron crystals” (PGECs).² The central point is to look for compounds that combine the low thermal conductivity of amorphous materials and the relatively low electrical resistivity and large thermopower of heavily doped semiconductors. Semiconducting clathrates based on group 14 elements have attracted much attention since Nolas et al. proposed germanium clathrates as potential PGEC candidates.³ Clathrates are comprised of a host framework of group 14 members and substituting elements that provide cavities stabilized by relatively large guest ions. Heat carrying acoustic phonons are effectively scattered on the guest atoms, which undergo low-frequency vibration. Consequently, the lattice thermal conductivities (κ_L) are extremely low and comparable to those in amorphous materials, where $\kappa_L \approx 1 \text{ W m}^{-1} \text{ K}^{-1}$.³ An overview of inorganic clathrates identified so far was recently presented in a review paper by Kovnir et al.⁴ It is hoped that an enhancement of the thermoelectric performance can be obtained through chemical modification and better control of composition, impurity phases, and bulk

morphology. Introduction of transition metals and rare earth elements into the structure might lead to larger effective band masses and sharp electron density of states ($g(\epsilon)$) features. To a first approximation, the thermopower (S) is proportional to the derivative of $g(\epsilon)$ with respect to the energy (ϵ) at the Fermi level (ϵ_F) ($S \propto (\partial g(\epsilon)/\partial \epsilon)_{\epsilon_F}$). Thus incorporation of transition metals or rare earth elements in the clathrate structure might improve thermoelectric performance.⁵ Cordier et al. first synthesized clathrates containing transition metals.⁶ Metallic and semiconducting behavior has been observed along with ferromagnetism in the germanium-based clathrates with substituted transition metals.⁷⁻¹⁴ Most studies focus on magnetic properties,⁷⁻¹⁰ and to the best of our knowledge, the only thorough studies of the transport properties of transition-metal-containing, germanium-based clathrates have been done by Anno et al. on several $\text{Ba}_8\text{TM}_y\text{Ga}_z\text{Ge}_{46-y-z}$ samples, where $\text{TM} = \text{Au, Cu, Pt, Pd}$.¹¹⁻¹⁴ In general, they found the TMs to preferentially occupy the 6c site of the host structure. Increases in the effective mass (m^*) and enhancement of the thermopower (S) were observed for the Pd- and Pt-substituted samples.^{12,13} For the Cu-containing

* Corresponding author: bo@chem.au.dk.

- (1) Ioffe, A. F. In *Semiconductor Thermoelements and Thermoelectric Cooling*; Infosearch Ltd: London, 1957.
- (2) Slack, G. A. *CRC Handbook of Thermoelectrics*; Rowe, D. M., Ed.; CRC: Boca Raton, FL, 1995; p 407.
- (3) Nolas, G. S.; Cohn, J. L.; Slack, G. A.; Schjuman, S. B. *Appl. Phys. Lett.* **1998**, *73*, 178.
- (4) Kovnir, K. A.; Shevelkov, A. V. *Russ. Chem. Rev.* **2004**, *73*, 923.

- (5) Mahan, G. D.; Sales, B.; Sharp, J. *Phys Today* **1997**, *50*, 42.
- (6) Cordier, G.; Woll, P. *J. Less Common Met.* **1991**, *169*, 291.
- (7) Hermann, R. F. W.; Tanigaki, K.; Kawaguchi, T.; Kuroshima, S.; Zhou, O. *Phys. Rev. B* **1999**, *60*, 13245.
- (8) Li, Y.; Chi, J.; Gou, W.; Khandekar, S.; Ross, J. H., Jr. *J. Phys.: Condens. Matter* **2003**, *15*, 5535.
- (9) Li, Y.; Ross, J. H., Jr. *Appl. Phys. Lett.* **2003**, *83*, 2868.
- (10) Kawaguchi, T.; Tanigaki, K.; Yasukawa, M. *Appl. Phys. Lett.* **2000**, *77*, 3438.
- (11) Anno, H.; Hokazono, M.; Takakura, H.; Matsubara, K. *Proc. Int. Conf. Thermoelectrics* **2005**, *XXIV*, 120.
- (12) Anno, H.; Hokazono, M.; Kawamura, M.; Matsubara, K. *Proc. Int. Conf. Thermoelectrics* **2003**, 121.
- (13) Hokazono, M.; Kawamura, M.; Anno, H.; Matsubara, K. *Trans. MRS-J.* **2004**, *29*, 2793–2796.
- (14) Hokazono, M.; Anno, H.; Matsubara, K. *Mater. Trans.* **2005**, *46*, 1485–1489.

Table 1. Selected Properties of the Synthesized Samples^a

	$x = 0.0$	$x = 0.1$	$x = 0.2$	$x = 0.3$	$x = 0.4$	$x = 0.5$	$x = 0.6$	$x = 0.7$
δ_{teo} (g cm ⁻³)	5.9617	5.9625	5.9633	5.9641	5.9650	5.9658	5.9666	5.9674
$\delta/\delta_{\text{teo}}$	0.922	0.974	0.980	0.977	0.973	0.977	0.975	0.972
a (Å)	10.6894(2)	10.69025(6)	10.69037(9)	10.69046(9)	10.69036(7)	10.69106(8)	NA	10.69145(5)
n (e uc ⁻¹)	0.054	0.041	0.075	0.111	0.188	0.175	0.182	0.206
μ_{H} (cm ² V ⁻¹ s ⁻¹)	3.40	8.81	9.57	9.91	7.68	9.33	9.78	9.01
m^*/m_e	0.495	0.967	1.06	1.10	1.21	1.09	1.14	1.11
$\rho_{400\text{K}}/\rho_{2\text{K}}$	0.0031	0.00045	0.124	0.837	1.05	1.23	1.14	1.34

^a The theoretical density (δ_{teo}) is calculated from a linear fit to the measured lattice parameter at room temperature (a), assuming that no vacancies are present and that the composition equals the nominal composition. The density δ , measured at room temperature, is given in fractions of δ_{teo} . The lattice constant, a , was obtained using conventional powder diffraction employing LaB₆ as an internal standard. The Hall carrier concentration (n) in units of electrons per unit cell, the mobility (μ_{H}), and the effective mass (m^*) are room-temperature values. m^* is calculated from the measured thermopower and n . $\rho_{400\text{K}}/\rho_{2\text{K}}$ is the residual resistance ratio, i.e., the resistivity at 400 K divided by the resistivity at 2 K.

samples, which were all n -type, no significant effects on m^* and S were observed. The mobility, however, increased significantly with increasing copper content. This was attributed to less disorder scattering because of the preferential ordering of the Cu atoms and the increasing molar content of Ge. In the present work, eight samples of nominal stoichiometry Ba₈Cu_{6-x}Ge_{40+x}, $x = 0-0.7$, have been synthesized to explore changes in the transport properties as a function of composition. The electrical transport properties of the samples are compared to theoretical values obtained from density functional calculations combined with semiclassical transport theory.

Experimental Section

The experimental details of the synthesis and the subsequent characterization are described below. Selected data are compiled in Table 1.

Synthesis. Eight Ba₈Cu_{6-x}Ge_{40+x} samples with $x = 0-0.7$ were synthesized. Initially, direct reaction of the elements was employed. However, problems with considerable germanium impurities led us to employ a novel method of synthesis. Barium and germanium was pre-reacted to form the Ba₆Ge₂₅ phase, which recently was shown to have a narrow phase width.¹⁶ Barium was added in a 10% surplus in order to compensate for evaporation losses and formation of nonequilibrium phases. The mixture was placed in a glassy carbon crucible inside a stainless steel bomb, which was sealed in an argon atmosphere. The bomb was heated to 900 °C, left to react for 2 h, and subsequently cooled slowly to an annealing temperature of 700 °C; when it reached this temperature, the mixture was quickly cooled. Ba₆Ge₂₅ is the only barium-rich phase that is resistant toward water and diluted acids. Consequently, impurity phases in Ba₆Ge₂₅ could be removed by immersion in such media. The powdered Ba₆Ge₂₅ was washed repeatedly with diluted acids in an ultrasonic bath. Single-phase Ba₆Ge₂₅ was confirmed by X-ray powder diffraction. Stoichiometric amounts of Ba₆Ge₂₅, Cu, and Ge were subsequently reacted in a quartz ampule sealed in an argon atmosphere. The ampule had been carbon-coated using high-temperature cracking of acetone. The mixture was heated to 1000 °C and subsequently cooled to an annealing temperature of 700 °C; when it reached this temperature, the mixture was quenched to room temperature. The as-synthesized bulk material was finely ground in a mortar and spark plasma sintering was used to obtain mechanically stable pellets for further characterization. The samples were compacted at a pressure of 75 MPa and a temperature of 725 °C. Heating rates were approximately 75 °C min⁻¹ and holding

times were 2–4 min. Samples were compacted to 3–4 mm high cylinders with a diameter of 12 mm. Sample densities were measured using an immersion technique on a home build device at 22 °C, where the density of immersion liquid (water) is 0.99786 g cm⁻³. The theoretical values were calculated using the nominal stoichiometries Ba₈Cu_{6-x}Ge_{40+x} and a lattice parameter $a(x) = 10.68971 \text{ \AA} + 0.00247x \text{ \AA}$ taken from a linear fit to experimental values (see Figure 3 below). Densities range from 97.2 to 98.0% of theoretical values, assuming that no vacancies are present, the exception being the $x = 0$ sample, which is only 92% compacted. This latter sample deviates from the general picture in many respects; nonetheless, we have included all the data of this sample to stress the importance of highly compacted samples. The samples exhibit a metallic luster and are of good mechanical strength. Only a minute Ge impurity phase was visible by conventional X-ray powder diffraction and there was a tendency for it to increase with x . Only diffraction data for the $x = 0.4$ and $x = 0.7$ samples could be refined with a Ge impurity phase, yielding Ge impurities of 1.8 and 3.8%, respectively (mass percentage). For the other samples, the Ge content was estimated to be less than 1 mass percent.

X-ray Diffraction. Conventional powder X-ray diffraction data were collected with monochromatized Cu K α 1 radiation on all samples using a Bruker D8 powder diffractometer at the Department of Chemistry, University of Aarhus. The measurements used LaB₆ as an internal standard. The sample with $x = 0.1$ was used for detailed synchrotron powder diffraction measurements. Powder particles with a homogeneous size were extracted from the finely ground sample by the following method. Ethanol and powder were thoroughly mixed and left to settle for 5 min. The particles in suspension were carefully pipetted off, leaving the precipitate, which was subsequently discarded. The suspension was left to settle for 10 min, and the precipitate thereof was used in the diffraction experiment. The powder was packed in 0.1 mm capillaries in order to minimize absorption. For high-temperature (> 300 K) measurements, a 0.2 mm capillary was used. Powder diffraction patterns were recorded using 0.481648(2) Å synchrotron radiation. The wavelength was determined using a CeO₂ standard ($a = 5.411102 \text{ \AA}$). Data were recorded using the large Debye–Scherrer camera with an imaging plate detector on the BL02B2 beamline at the Spring-8 synchrotron radiation research facility. Low- and high-temperature setups included a N₂/hot air gas flow system with temperature ranges of 90–300 and 300–1000 K, respectively.

Physical Properties. Transport properties were measured on a Quantum Design physical property measurement system (PPMS) using the thermal transport option (TTO) and the AC transport option (ACT). Resistivity (ρ), thermal conductivity (κ), and thermopower (S) is measured simultaneously in the TTO. ρ is measured using a standard four-point setup, κ and S using the quasi-static technique employed in the TTO.¹⁷ The Hall resistivity (ρ_{H})

(15) Huo, D.; Sasakawa, T.; Muro, Y.; Takabatake, T. *Appl. Phys. Lett.* **2003**, *82*, 2640–2642.

(16) Carrillo-Cabrera, W.; Budnyk, S.; Prots, Y.; Grin, Y. Z. *Anorg. Allg. Chem.* **2004**, *630*, 2267.

(17) Maldonado, O. *Cryogenics* **1992**, *32*, 908.

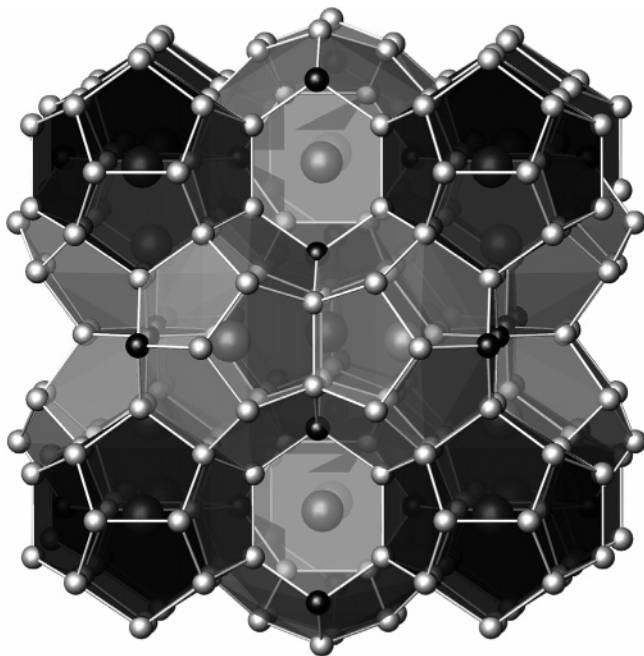


Figure 1. Ordered structure of $\text{Ba}_8\text{Cu}_6\text{Ge}_{40}$ with Cu on the $6c$ site and Ge occupying the remaining framework sites ($16i$ and $24k$). Barium is located at the $2a$ and $6d$ sites in two distinct framework cages: Ge_{20} (black dodecahedra) and $\text{Ge}_{20}\text{Cu}_4$ (gray tetrakaidecahedra).

was measured as function of the magnetic field (B) in 1 T steps. At each magnetic field, ρ_H is measured at 0 and 180° perpendicular to the field in order to eliminate the resistive part of the signal. For all samples, ρ_H is linear with field and R_H is determined from $\rho_H = R_H B$.

Computational Method. The calculations were performed using the L/APW+lo method¹⁸ as implemented in the WIEN2k code.¹⁹ A plane wave cutoff defined by $\min(R\alpha)\max(kn) = 5.6$ and sphere sizes of 2.5 au (Ba), 2.45 (Cu), and 2.1 au (Ge) were used. The Perdew–Burke–Ernzerhof (PBE) generalized gradient approximation (GGA)²⁰ was used for the exchange–correlation potential. For a better estimate of the band gap, one calculation using the Engel–Vosko (EV) GGA²¹ was also performed. 10 k-points on a shifted mesh in the irreducible Brillouin zone (IBZ) were used for the self-consistent field calculations, whereas 220 k-points on a nonshifted mesh in the IBZ were used for the transport calculations. For the calculations of the derivatives necessary for the transport coefficients, we used the program BoltzTrap.²² The original k mesh was interpolated onto a mesh five times as dense.

Results and Discussion

Structure. $\text{Ba}_8\text{Cu}_6\text{Ge}_{40}$ crystallizes in a type I clathrate structure ($Pm\bar{3}n$ space group) with a reported lattice parameter of $a = 10.6859(8)$ Å.⁶ The framework consists of sp^3 -bonded germanium and copper. There are three distinct framework sites: $6c$, $16i$, and $24k$, named according to their space group symmetry. Figure 1 shows a fully ordered

structure of $\text{Ba}_8\text{Cu}_6\text{Ge}_{40}$, where Cu atoms reside on the $6c$ sites. The barium atoms are surrounded by 20 and 24 framework atoms for the $2a$ and $6d$ sites, respectively. Cordier et al.⁶ found transition metals to preferentially occupy the $6c$ site. This was confirmed by Li et al.⁸ in their study of $\text{Ba}_8\text{Cu}_x\text{Ge}_{46-x}$, where $x = 2, 4, 6$, but they noticed a deviation from the 6:40 Cu:Ge composition to approximately 5:41, regardless of starting composition. This is in better agreement with Zintl–Klemm expectations, assuming the oxidation states of Ba, Cu, and Ge to be II, I, and IV, respectively. Furthermore, Li et al. also suggested the existence of vacancies.⁸ Structural refinements were done using the Fullprof package.²³ The background was modeled using linear interpolation between refineable background points. Because of the small difference in X-ray contrast between Cu and Ge, the stoichiometry is difficult to refine. The occupancies correlate strongly with other parameters, notably the thermal parameters. Consequently, no Cu occupancies were allowed on the $16i$ and $24k$ site, and the Ba occupancies were fixed at 100%. The refined occupancies can be seen in Table 3 and sum up to a stoichiometry of $\text{Ba}_8\text{Cu}_{4.61}\text{Ge}_{40.84}\square_{0.56}$. The vacancies found in the refinement on the $16i$ and $24k$ sites might partly stem from Cu being present on these sites. Cu has three fewer electrons than Ge, and a Cu occupancy can thus be modeled by lowering the Ge occupancy and introducing vacancies. There seems to be some degree of ordering in $M_8\text{Ga}_{16}\text{Ge}_{30}$, where $M = \text{Sr}, \text{Ba}, \text{Eu}$. As an example, gallium has a preference for the $6c$ site and avoids the $16i$ site in $\text{Ba}_8\text{Ga}_{16}\text{Ge}_{30}$ and $\text{Sr}_8\text{Ga}_{16}\text{Ge}_{30}$.^{24,25} However, to the best of our knowledge, a full ordering has not been observed. Because $\text{Ba}_8\text{Cu}_6\text{Ge}_{40}$ possesses a high degree of ordering, studying this compound in relation to the mentioned disordered structures might shed further light on how the framework structure influences the transport properties.

Structural Properties. Crystal structure and physical properties are intimately linked. A multi-temperature synchrotron powder diffraction study was undertaken in order to gain further knowledge about site occupancy, stoichiometry, and thermal behavior of the structure. The $x = 0.1$ sample was chosen for the diffraction experiment. The sample had a small germanium impurity (mass fraction of 0.29% obtained by Rietveld refinement), but no Ba- or Cu-containing impurity phases are visible in the pattern (Figure 2). This confirms that the chosen method of synthesis yields single-phase samples with minute impurities. High-temperature diffraction patterns were recorded with a $\Delta T = 40$ K interval from 300 to 980 K. A partial thermal decomposition starting at approximately 700 K was observed, which might pose a threat to the potential application of the compound as a high-temperature thermoelectric. Carrillo-Cabrera et al. have made a thorough study of the germanium-rich part of the Ba–Ge binary phase diagram.¹⁶ They report on a metastable phase with approximate composition BaGe_5

(18) Madsen, G. K. H.; Blaha, P.; Schwarz, K.; Sjostedt, E.; Nordstrom, L. *Phys. Rev. B* **2001**, *64*, 195134.

(19) Blaha, P.; Schwarz, K.; Madsen, G. K. H.; Kvasnicka, D.; Luitz, J. In *WIEN2k, An augmented Plane Wave Plus Local Orbitals Program for Calculating Crystal Properties*; Vienna University of Technology: Vienna, Austria, 2001.

(20) Perdew, J. P.; Burke, K.; Ernzerhof, M. *Phys. Rev. Lett.* **1996**, *77*, 3865.

(21) Engel, E.; Vosko, S. H. *Phys. Rev. B* **1993**, *47*, 13164.

(22) Madsen, G. K. H.; Singh, D. J. *Comput. Phys. Commun.* **2006**, *175*, 67–71.

(23) Rodriguez-Carvajal, J. *Physica B* **1993**, *192*, 55.

(24) Benti, A.; Palmqvist, A. E. C.; Bryan, J. D.; Latturmer, S.; Stucky, G. D.; Furenli, L.; Iversen, B. B. *Angew. Chem., Int. Ed.* **2000**, *39*, 3613.

(25) Zhang, Y.; Lee, P. L.; Nolas, G. S.; Wilkinson, A. P. *Appl. Phys. Lett.* **2002**, *80*, 2931.

Table 2. Refined Parameters from the Rietveld Refinement on 15 Synchrotron Radiation (using $\lambda = 0.481648(2)$ Å) Data Sets on $\text{Ba}_8\text{Cu}_{5.9}\text{Ge}_{40.1}$ Covering the Temperature Range 90–300 K^a

T (K)	R_p	R_{wp}	χ^2	U_{11} (2a)	U_{11} (6d)	U_{22} (6d)	x,y,z 16i	y 24k	z 24k	a
90	1.59	2.33	1.75	25(2)	99(5)	200(4)	0.18320(1)	0.31483(1)	0.11941(1)	10.66591(2)
105	1.62	2.38	1.72	36(2)	113(5)	208(4)	0.18322(1)	0.31480(1)	0.11936(1)	10.66785(2)
120	1.61	2.38	1.71	38(2)	113(5)	228(4)	0.18322(1)	0.31486(1)	0.11931(1)	10.66978(2)
135	1.61	2.37	1.66	44(2)	120(5)	237(4)	0.18320(1)	0.31484(1)	0.11940(1)	10.67157(2)
150	1.60	2.35	1.63	49(2)	130(5)	249(4)	0.18318(1)	0.31478(1)	0.11940(1)	10.67364(2)
165	1.61	2.38	1.62	52(2)	135(5)	267(4)	0.18320(1)	0.31481(1)	0.11942(1)	10.67579(2)
180	1.60	2.35	1.57	54(3)	144(5)	277(4)	0.18322(1)	0.31482(1)	0.11945(1)	10.67773(2)
195	1.59	2.34	1.54	57(3)	149(5)	290(4)	0.18319(1)	0.31476(1)	0.11947(1)	10.67969(2)
210	1.57	2.34	1.50	63(3)	155(6)	297(4)	0.18327(1)	0.31470(1)	0.11940(1)	10.68159(2)
225	1.61	2.38	1.53	67(3)	156(6)	311(4)	0.18323(1)	0.31473(1)	0.11935(1)	10.68365(2)
240	1.62	2.38	1.51	72(3)	168(6)	325(4)	0.18324(1)	0.31469(1)	0.11939(1)	10.68579(2)
255	1.66	2.44	1.54	77(3)	163(6)	344(4)	0.18323(1)	0.31471(1)	0.11936(1)	10.68795(2)
270	1.68	2.45	1.51	85(3)	175(6)	354(5)	0.18324(1)	0.31475(1)	0.11937(1)	10.69010(2)
285	1.67	2.43	1.46	88(3)	189(7)	362(5)	0.18324(1)	0.31465(1)	0.11942(1)	10.69222(2)
300	1.71	2.53	1.58	97(3)	182(7)	376(5)	0.18327(1)	0.31477(1)	0.11940(1)	10.69439(3)

^a R_p , R_{wp} and χ^2 are the profile factor, weighted profile factor, and chi square provided by the FullProf program, respectively.²³ The anisotropic temperature parameters are given for the two crystallographically unique barium atom and are in units of $1 \times 10^{-4} \text{ \AA}^2$. $U_{11} = U_{22} = U_{33}$ for Ba on 2a and $U_{22} = U_{33}$ for Ba 6d. Refined positions are given for the 16i and 24k sites in units of the lattice parameter a . The lattice parameter a is given in Å.

Table 3. Refined Occupancies in $\text{Ba}_8\text{Cu}_{5.9}\text{Ge}_{40.1}$ Obtained From the Data Set Recorded at 90 K

site	Cu	Ge	□
6c	0.767(15)	0.199(14)	0.033(20)
16i	0	0.9852(2)	0.0148(2)
24k	0	0.9949(2)	0.0051(2)

□ denotes a vacancy.

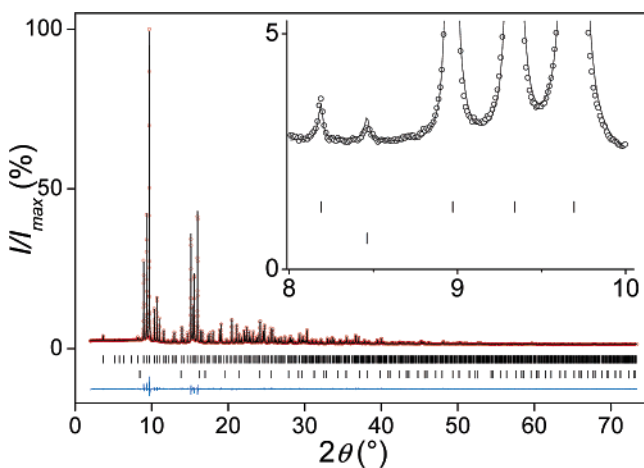


Figure 2. Rietveld refinements of synchrotron powder diffraction pattern. The inset is a zoom on the region $8^\circ < 2\theta < 10^\circ$ and the tiny peak at approximately 8.5° is attributable to a 0.29% mass fraction germanium impurity.

forming in the temperature range 723–881 K. Future studies will hopefully reveal whether the formation of this compound is the cause of the thermal decomposition. Barium is primarily rattling in the large $\text{Ge}_{20}\text{Cu}_4$ cage surrounding the 6d positions (gray cage in Figure 1). The barium atom in the large cage can be modeled as an Einstein oscillator. In the Einstein model, the ADPs are given by

$$U_{ii} = \frac{\hbar^2}{2mk_B\theta_{E,ii}} \coth\left(\frac{\theta_{E,ii}}{2T}\right) + d_{ii}^2 \quad (1)$$

Possible temperature-independent disorder is described by d , and θ_E is the Einstein temperature. To a first approximation, d consists of two contributions. One comes from off-center positioning of Ba, whereas the other stems from differences in the local compositions of the cages.²⁶ Fitting

Table 4. Atomic Displacements Parameters (U_{ii}) and Lattice Parameter (a) at 300 K as Well as Einstein Temperatures (θ_E) and Temperature-Independent Disorder Parameters (d) of $\text{Ba}_8\text{Cu}_{5.9}\text{Ge}_{40.1}$ ^a

	$\text{Ba}_8\text{Ge}_{43}$ ^b	$\text{Ba}_8\text{Cu}_6\text{Ge}_{40}$	$\text{Ba}_8\text{Ga}_{16}\text{Ge}_{30}$ ^c
a (Å)	10.6565(2) ^d	10.69441(2)	10.76388(5)
U_{11} (Å ²)	0.0159(3)	0.0182(7)	0.0175(5)
U_{22} (Å ²)	0.0286(2)	0.0376(5)	0.0448(4)
$\theta_{E,11}$ (K)	N/A	92(2)	101
$\theta_{E,22}$ (K)	N/A	64.3(4)	73
d_{11} (Å)	N/A	0.080(2)	0.081
d_{22} (Å)	N/A	0.109(1)	0.157

^a The corresponding values for $\text{Ba}_8\text{Ga}_{16}\text{Ge}_{30}$ and $\text{Ba}_8\text{Ge}_{43}$ are shown for comparison. ^b Data taken from Carrillo-Cabrera et al.¹⁶ ^c Data taken from Bontien et al.²⁸ ^d $\text{Ba}_8\text{Ge}_{43}$ was recently shown to have a superstructure.¹⁶

the ADPs for the barium atom in the large cage gives the θ_E and d parameters shown in Table 4. The d_{11} , $\theta_{E,11}$, and $\theta_{E,22}$ values obtained for $\text{Ba}_8\text{Cu}_6\text{Ge}_{40}$ are similar to the corresponding values for $\text{Ba}_8\text{Ga}_{16}\text{Ge}_{30}$. However, the d_{22} ($= d_{33}$) parameters are different for the two. The difference in d_{22} could be interpreted as an indication of a greater ordering of the framework atoms in $\text{Ba}_8\text{Cu}_6\text{Ge}_{40}$ compared to $\text{Ba}_8\text{Ga}_{16}\text{Ge}_{30}$. In $\text{Ba}_8\text{Cu}_6\text{Ge}_{40}$, Cu is primarily located on 6c sites, whereas Ge is mainly distributed over the 16i and 24k sites. In $\text{Ba}_8\text{Ga}_{16}\text{Ge}_{30}$, $\text{Sr}_8\text{Ga}_{16}\text{Ge}_{30}$, $\text{Ba}_8\text{Ga}_{16}\text{Si}_{30}$, and $\text{Ba}_8\text{In}_{16}\text{Ge}_{30}$ the framework atoms order only partially.^{24–26} The local composition of the cages thus might be more homogeneous in $\text{Ba}_8\text{Cu}_6\text{Ge}_{40}$, leading to a smaller d_{22} . Why the d_{11} parameter does not change is unclear. This would be expected, when the order increases. Investigating the local environment of the cages is complex, and a quantitative comparison of the $\text{Ba}_8\text{Ga}_{16}\text{Ge}_{30}$ and $\text{Ba}_8\text{Cu}_6\text{Ge}_{40}$ would require detailed knowledge about the Cu, Ga, and Ge distribution, and at least for $\text{Ba}_8\text{Ga}_{16}\text{Ge}_{30}$, this is not known. The smaller d_{22} parameter might also partly reflect the change in lattice parameter. There is some evidence for off-center positioning in $\text{Ba}_8\text{Ga}_{16}\text{Ge}_{30}$.^{24,27} This might not be present in $\text{Ba}_8\text{Cu}_6\text{Ge}_{40}$ because of a smaller lattice parameter.

(26) Bontien, A.; Nishibori, E.; Paschen, S.; Iversen, B. B. *Phys. Rev. B* **2005**, *71*, 144107.

(27) Paschen, S.; Carrillo-Cabrera, W.; Bontien, A.; Tran, V. H.; Baenitz, M.; Grin, Y.; Steglich, F. *Phys. Rev. B* **2001**, *64*, 214404.

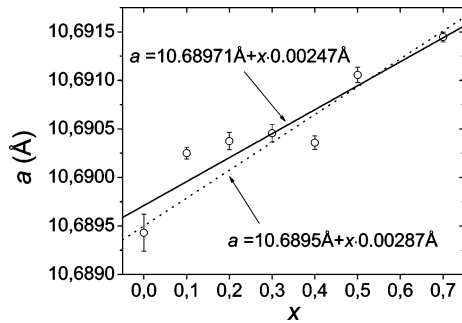


Figure 3. Experimentally determined lattice parameter (a) as a function of x . The dotted line shown is a relation between a and x calculated from data by Li et al. using a least-squares fit (an offset in a of 0.00245 Å has been added).⁸ The solid line is a least-squares fit to the data presented here.

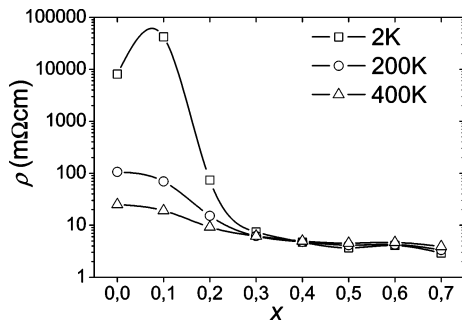


Figure 4. Resistivity (ρ) at 2, 200, and 400 K as a function of x . A systematic change from semiconducting to metallic behavior is seen upon increasing x .

Stoichiometry Dependence of Lattice Constants. Conventional powder diffraction patterns were recorded employing an internal standard (LaB_6). This allows for quantitative comparison of very small lattice parameter deviations. Rietveld refinements including both phases were carried out, and the determined lattice parameters are shown in Figure 3 as a function of x . The relationship between a and x is not entirely systematic. There is, however, a tendency for a to increase with increasing x . Li et al. have determined lattice parameters for $x = 0-4$ in steps of 2.⁸ From their data, the lattice parameter is found to decrease by 0.00287 Å per extra Cu added per unit cell (uc) ($\partial a/\partial x = 0.00287$ Å). This relation is the dotted line in Figure 3 (an arbitrary constant has been added), and the agreement with our data is fair. The solid line is obtained by least squares refinement on our data.

Transport Properties

Resistivity. For small x , the samples are semiconducting, but upon increasing x , the samples become more and more metallic in character, as evident from Figure 4. In Figure 5, the thermal dependence of the resistivity is shown for all samples along with graphs exhibiting different thermal dependencies. The systematic dependence of ρ upon x can readily be seen from Figure 4. Intrinsic conduction ($\ln \rho \propto T^{-1}$) cannot solely explain the observed resistivity for the semiconducting samples. Clearly, the data show different power dependencies on temperature, Figure 5.

Thermal Conductivity. Among the inorganic clathrates, some structures exhibit a glasslike thermal conductivity temperature dependence, whereas others show a normal crystal-like temperature dependence.²⁸ In Figure 6, the lattice

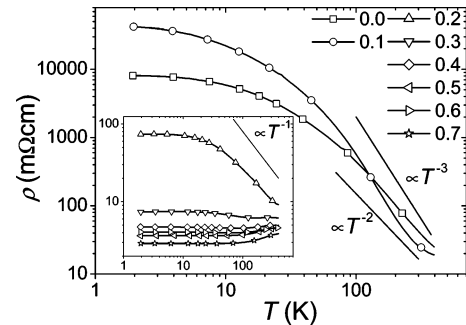


Figure 5. Resistivities (ρ) of the samples as a function of T along with graphs showing different power dependencies. Only every 20th data point is shown.

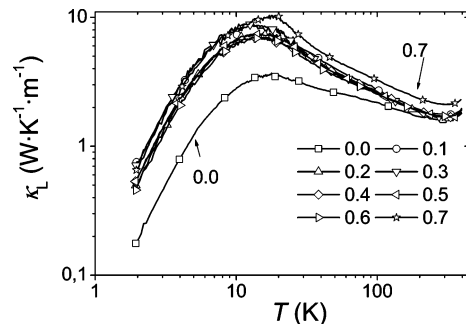


Figure 6. Lattice thermal conductivity (κ_L) of the synthesized samples. The subtracted electronic contribution has been estimated by the Wiedemann–Franz law. Only every 20th data point is shown.

thermal conductivity (κ_L) is shown and the samples all exhibit a crystal-like temperature dependence. The subtracted electronic contribution (κ_e) is estimated using the Wiedemann–Franz law $\kappa_e = LT/\rho$, where L is the Lorentz number. In the case of degenerate charge carriers, $L = L_0 = \pi^2/3(k_B/e)^2$. For nondegenerate charge carriers, L depends on the scattering mechanism. There are probably several scattering mechanisms contributing to the thermal resistivity, and an exact evaluation of L is impossible. Consequently, it is assumed that $L = L_0$. Overall, κ_L is observed to be almost independent of the Cu:Ge composition. Nonetheless, two samples deviate from the general picture, namely, the $x = 0.0$, especially at low temperature, and the $x = 0.7$ at temperatures above approximately 10 K. The deviation can be explained by a poor sample quality in the case of the $x = 0.0$ sample. The sample had not been fully compacted (92%), as is evident from the densities shown in Table 1. An increasing grain boundary scattering with decreasing temperature due to porosity can therefore be expected. This agrees well with the observation that the relative difference between the $x = 0.0$ sample and the other samples increases as the temperature decreases. The $x = 0.7$ sample has a significant germanium impurity that might influence κ_L because crystalline germanium has a thermal conductivity of around 60 $W m^{-1} K^{-1}$ at room temperature. Thus, even small fractions might induce changes in κ_L . The lattice thermal conductivity of the samples is around 1.9 $W m^{-1} K^{-1}$ at 200 K; this is significantly higher than that for $Ba_8Ga_{16}Ge_{30}$, which has a lattice thermal conductivity of around

(28) Bontien, A.; Christensen, M.; Bryan, J. D.; Sanchez, A.; Paschen, S.; Steglich, F.; Stucky, G. D.; Iversen, B. B. *Phys. Rev. B* **2004**, *69*, 045107.

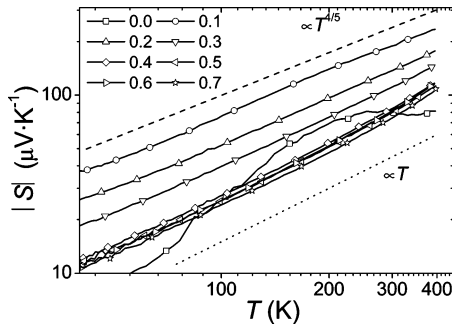


Figure 7. Thermal dependence of the thermopower (S) for the synthesized samples. Different power dependencies are indicated by the added graphs. Only every 8th data point is shown.

$1 \text{ W m}^{-1} \text{ K}^{-1}$ at 200 K .²⁷ Less disorder in $\text{Ba}_8\text{Cu}_6\text{Ge}_{40}$ due to Cu mainly occupying the $6c$ sites might account for this difference.

Thermopower. Figure 7 shows $|S|$ as function of temperature. The apparent systematic manner in which $S(T)$ changes (Figure 7) can have several possible explanations. If a single scattering mechanism dominates and a rigid and parabolic band model is assumed, it is possible to derive the following expression for S

$$S = \frac{\pi^2 k_B^2 T (r + 3/2)}{3e \epsilon_F} = \frac{2m^* \pi^2 k_B^2 T (r + 3/2)}{3e \hbar^2 (3\pi^2 n)^{2/3}} \quad (2)$$

Here, n is the charge-carrier concentration. It is assumed that the relaxation time (τ) has an exponential dependence on the energy given by $\tau \propto e^r$, where r is dependent on the scattering mechanism. For impurity and phonon scattering, $r = 3/2$ and $-1/2$, respectively. If the same scattering mechanism is dominant over the studied temperature range, a linear $S(T)$ can be expected, provided the other constituting variables are constant. If the charge-carrier concentration is temperature-dependent, S cannot be linearly dependent on T . The almost linear $S(T)$ for small x is at variance with the relatively large magnitude of S and the fact that samples with $x = 0-0.3$ have semiconducting temperature dependencies of the electrical resistivity. The increasing metallic character of the samples observed in the resistivity measurements is reflected in the thermopower that changes from a $T^{0.8}$ dependence in the case of $x = 0.1$ to a T^1 dependence for higher x . A linear temperature dependence is typically seen in metallic systems where the charge-carrier concentration is constant. Unfortunately Hall measurements were done only at room temperature. In principle, the Hall data are independent of τ . Multi-temperature measurements of the Hall coefficient to subsequently yield $n(T)$ could shed further light onto the scattering mechanism involved.

Hall Carrier Concentration and Mobility. Figure 9 shows the Hall carriers per uc as a function of x . The expected behavior of n is not followed. n varies only slightly from 0.05 to 0.2, but in a systematic manner, i.e., n increases with increasing x . Figure 10 shows the room-temperature Hall mobilities $\mu_H = R_H/\rho$ for the synthesized samples. The low-density $x = 0$ sample deviates from the others, which all have mobilities in the range $7.5-10 \text{ cm}^2 \text{ V}^{-1} \text{ s}^{-1}$. These values are comparable to the values obtained for $M_8\text{Ga}_{16}\text{Ge}_{30}$, $M = \text{Ba, Eu, Sr}$,^{12,29} and apparently Cu substitution

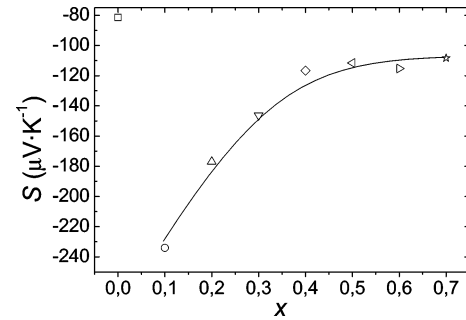


Figure 8. Thermopower (S) at 395 K as a function of the substitution x .

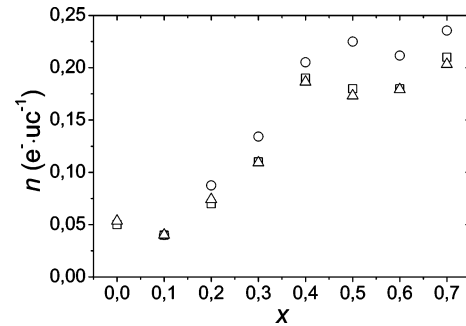


Figure 9. Carriers per unit cell as a function of x . The squares are evaluated directly from the experimental Hall coefficient at room temperature, assuming parabolic bands. The circles are evaluated by comparing the calculated doping dependence of the thermopower with the experimental. The triangles are evaluated by comparing the experimental Hall coefficients with the calculated.

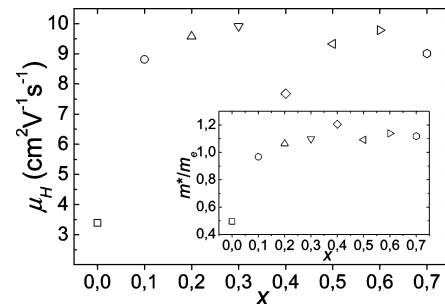


Figure 10. Mobility (μ_H) as a function of x . Inset shows the density of states effective mass (m^*) in units of the electron mass at 300 K as a function of x .

does not seem to affect the mobility notably. This is in contradiction to the findings of Anno et al., who found that increasing the Cu content in $\text{Ba}_8\text{Cu}_x\text{Ga}_{16-3x}\text{Ge}_{30+2x}$ increased the mobility. Using eq 2 and assuming acoustic phonon scattering ($r = -1/2$), we can estimate m^* ; these values are shown as an inset in Figure 10. They are quite similar to the ones found for n -type $\text{Ba}_8\text{Ga}_{16}\text{Ge}_{30}$,¹² indicating that the d orbitals from the substituted copper contribute negligibly to $g(\epsilon)$ near the Fermi level in our samples.

Band Structure

Fully Occupied Model. Before looking at $g(\epsilon)$, it is worth analyzing the bonding qualitatively from the Zintl–Klemm concept.³⁰ The tetrahedrally bonded framework of group 14 members and substituting elements is charge-compensated

(29) Paschen, S.; Pacheco, V.; Bentien, A.; Sanchez, A.; Carrillo-Cabrera, W.; Baenitz, M.; Iversen, B. B.; Grin, Y.; Steglich, F. *Physica B* **2003**, 328, 39.

(30) Schäfer, H. *Annu. Rev. Mater. Sci.* **1985**, 15, 1.

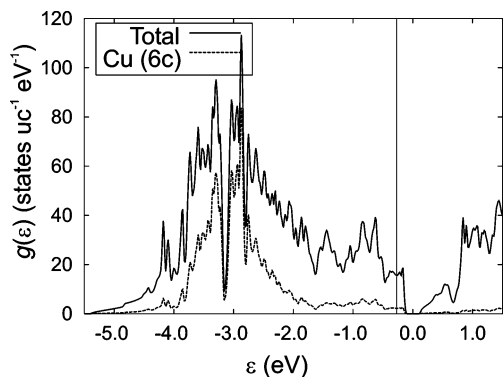


Figure 11. Calculated density of states for ordered $\text{Ba}_8\text{Cu}_6\text{Ge}_{40}$ with all Cu on the 6c site. The dashed line shows the Cu contribution to the total density of states (black line). The d character is most pronounced well below the band gap. The vertical line shows the Fermi level of the nominal $\text{Ba}_8\text{Cu}_6\text{Ge}_{40}$ compound. The plot has been calculated using the PBE functional, which gives a gap of approximately 0.19 eV between the valence bands and the conduction bands. When using the EV functional, we obtain a gap of 0.52 eV.

by the guest atoms.^{6,31} There are 46 framework atoms per uc and 92 covalent sp^3 bonds. Thus, $\text{Ba}_8\text{Cu}_6\text{Ge}_{40}$ is expected to have 184 states in both the valence and the conduction band. The barium atom donates its valence electrons to the tetrahedrally bonded framework, and stoichiometric $\text{Ba}(\text{II})_8\text{Cu}(\text{I})_6\text{Ge}(\text{IV})_{40}$ therefore has 182 valence electrons per unit cell if the elements are in the assigned valence states. Apart from the 184 bonding states, the valence bands contain 60 d states 2–4 eV below the Fermi level located on the Cu atoms, Figure 11. A splitting in energy of the d contribution is seen because of the tetrahedral environment. Furthermore, there is a small hybridization between the d states and the valence bands. It is interesting to note that this hybridization is almost absent in the conduction bands, meaning that there is no d contribution to the states just above the gap. The calculated $g(\epsilon)$ is plotted in Figure 11. The Fermi level for the nominal $\text{Ba}_8\text{Cu}_6\text{Ge}_{40}$ stoichiometry is found in the valence bands, and the states between the Fermi level and the gap sum to exactly two electrons. The calculations thus confirm the Zintl electron counting and the valence states for Ba, Cu, and Ge to be II, I, and IV, in that order. Between the valence bands and the conduction bands, there is a gap of approximately 0.19 eV. Most GGA functionals yield band gaps that are smaller than the experimental. Empirically, it has been found that the EV functional²¹ yield gaps are in closer agreement with the experimental values.³² As an example, a predicted band gap of 0.4 eV for the type VIII $\text{Eu}_8\text{Ga}_{16}\text{Ge}_{30}$ clathrate³² was subsequently confirmed experimentally.³³ Applying the EV functional to $\text{Ba}_8\text{Cu}_6\text{Ge}_{40}$ gives a gap between the valence bands and conduction bands of 0.52 eV. It is clear that the calculated $g(\epsilon)$ agrees well with our expectations from the Zintl–Klemm concept. However, it agrees poorly with the observed transport properties. From $g(\epsilon)$ and the above Zintl–Klemm analysis, one would expect the number of carriers (in units of carriers per uc) to be given

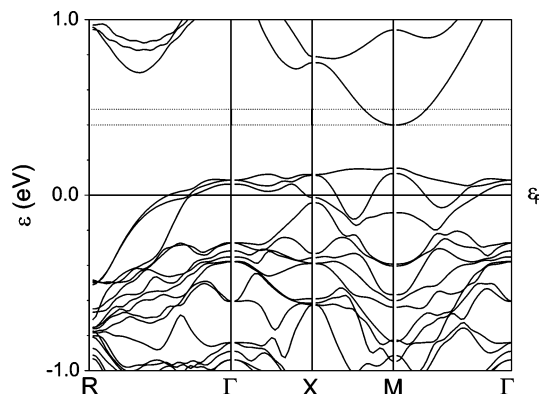


Figure 12. Calculated band structure for ordered $\text{Ba}_8\text{Cu}_6\text{Ge}_{40}$. The points are labeled as R = (1, 1, 1), X = (1, 0, 0), and M = (1, 1, 0) with respect to $\pi(a^*, b^*, c^*)$. The dotted lines mark the chemical potentials at 300 K that correspond to the doping range achieved experimentally.

as $n(x) = -3x + 2$. Thus a *p*-type metal with around two carriers per uc would be expected for $x = 0.0$. With increasing x , the number of *p* carriers should drop, and for $x = 0.7$, one would expect 0.1 *n* carriers per uc. In contrast, several of the samples clearly show a semiconducting behavior, Figures 4 and 5, and all of the samples have *n*-type properties, Figures 8 and 9. Furthermore, the Hall carrier concentration varies only between 0.05 and 0.25 carriers per uc, Figure 9. If the Fermi level was situated in the valence band, an increase in m^* would be expected on the basis of the significant contribution from Cu d orbitals to $g(\epsilon)$. This does not agree with the $m/m^* \approx 1$ that was derived above. The measured transport coefficients can therefore not be explained by a fully occupied, ordered model. Instead, Figure 12 shows that the conduction bands near the gap are dominated by a single parabolic band, which would agree well with the observed transport coefficients. We will now argue that vacancy formation can place the chemical potential in the conduction bands, and interpret the transport properties using the parabolic conduction band. Finally, we will discuss how the vacancy formation can be interpreted in terms of stoichiometry.

Vacancy Formation. Structural vacancies are well-known among the clathrates, e.g., in $\text{Ba}_8\text{Ge}_{43}\square_3$ (\square denotes a vacancy) and $\text{Rb}_8\text{Sn}_{44}\square_2$, where ordering of the vacancies results in a superstructure.^{17,34} Vacancies in $\text{Ba}_8\text{Cu}_6\text{Ge}_{40}$ are thus quite plausible. A vacancy within the tetrahedrally bonded framework would leave four dangling bonds (DB). This corresponds to eight states, two from each bond, with energy levels that can be assumed to lie within the band gap due to their nonbonding nature.³⁵ Myles et al. did a computational comparison of $\text{Cs}_8\text{Sn}_{46}$ and $\text{Cs}_8\text{Sn}_{44}\square_2$.³⁵ They found DB states forming within the band gap of $\text{Cs}_8\text{Sn}_{46}$ when vacancies were introduced, and the band gap width of $\text{Cs}_8\text{Sn}_{44}\square_2$ was reduced with respect to that of $\text{Cs}_8\text{Sn}_{46}$.³⁶ We have calculated the band structure for $\text{Ba}_8\text{Cu}_5\text{Ge}_{40}\square_1$, where vacancies are assumed to occupy the 6c site (vacancies in $\text{Ba}_8\text{Ge}_{43}\square_3$ and $\text{Rb}_8\text{Sn}_{44}\square_2$ are located on the 6c site^{17,34}). The result is shown in Figure 13 together with the underlying

(31) Kuhl, B.; Czybulka, A.; Schuster, H. U. *Z. Anorg. Allg. Chem.* **1995**, *621*, 1.

(32) Madsen, G. K. H.; Schwarz, K.; Blaha, P.; Singh, D. J. *Phys. Rev. B* **2003**, *68*, 125212.

(33) Sichelschmidt, J.; Voevodin, V.; Pacheco, V.; Grin, Y.; Steglich, F.; Nishi, T.; Kimura, S. *Eur. Phys. J. B* **2005**, *46*, 363.

(34) Dubois, F.; Fässler, T. F. *J. Am. Chem. Soc.* **2005**, *127*, 3264.

(35) Mott, N. F. In *Conduction in Noncrystalline Materials*; Clarendon Press: Oxford, U.K., 1987.

(36) Myles, C. W.; Dong, J.; Sankey, O. F. *Phys. Rev. B* **2001**, *64*, 165202.

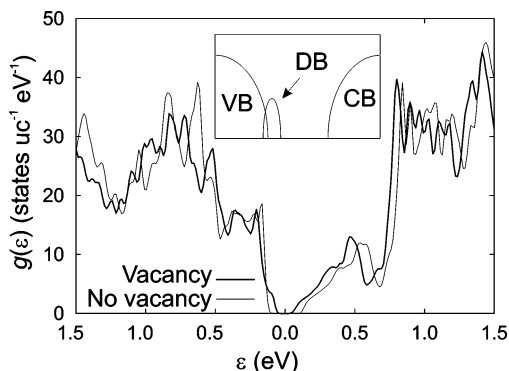


Figure 13. Calculated density of states ($g(\epsilon)$) for ordered $\text{Ba}_8\text{Cu}_5\text{Ge}_{40}\square_1$, with Cu and the vacancy (\square) occupying the $6c$ site (black curve). The underlying gray curve for the vacancy free model from Figure 11 is shown for comparison. The zero points have been placed in the gaps. The insert shows a schematic representation of $g(\epsilon)$ for a clathrate containing vacancies. Dangling bond (DB) states form at the top of the valence band (VB), whereas the conduction band (CB) remains unaltered.

vacancy-free model. In the vacancy-free model, the calculated band gap is 0.19 eV, whereas in the clathrate with vacancies, the band gap is 0.06 eV. As is evident from Figure 13, the DB states are localized at the top of the valence band: The shape of the conduction band is not altered and integration of $g(\epsilon)$ to the band gap yields 184 states i.e., 176 bonding states and eight DB states. A qualitative illustration of the situation is depicted in the inset of Figure 13. The description of the vacancies employed here is very crude and consequently the energy distribution of the DB states can be questioned. Whether they are energetically situated just above the valence band, in the middle of the gap, or at the bottom of the conduction band is an open question. The point is that a large concentration of vacancies would shift the chemical potential to the gap. In the following, we will therefore interpret the conductivity in terms of the conduction bands, which at the gap are dominated by a single parabolic-like band. It is seen that this can give a clear interpretation of the experimental measurements.

Thermopower and Hall Coefficients. In the constant τ approximation, both the calculated thermopower and Hall coefficients are τ independent.²² Therefore, the doping of each of the eight experimental samples can be estimated by comparison with the experimentally measured coefficients, Figure 9. It is seen that the estimations based on the thermopower and Hall coefficients are in very good agreement and also agree with the doping estimated from $R_H = 1/(ne)$. The dotted lines in Figure 12 show the chemical potentials that lead to the calculated Hall coefficients at 300 K. The transport should thus be dominated by the parabolic conduction band, which agrees well with several observations: the effective masses close to m_e , negative carrier signs, and the semiconductor behavior of the $x = 0.0$ – 0.2 samples.

Resistivity. There is a discrepancy between the relatively large charge carrier concentration and the semiconducting behavior found in the $x = 0$ – 0.3 samples. Applying textbook semiconductor physics and assuming the $x = 0.1$ sample is an intrinsic semiconductor (this is justified by the small $\rho_{400\text{K}}/\rho_{2\text{K}}$, see Table 1), we find that the charge-carrier concentration at 300 K would correspond to a semiconductor with a band gap of less than 0.01 eV. This is at variance with the

above-mentioned calculations that show band gaps at least an order of magnitude larger. Both polycrystalline and single-crystalline germanium-based clathrates are found to have low mobilities.^{11–14,37–39} Less than 1 vacancy per unit cell will not increase the scattering rate significantly and consequently will not seriously affect the mobility. Vacancies, therefore, cannot be directly responsible for the observed behavior, but a vacancy does give rise to dangling bonds with highly localized states.³⁵ Thermally activated electron hopping between localized states ($\ln(\rho) \propto T^{-1/4}$) cannot solely account for the observed resistivity. The resistivity might be a combination of intrinsic conduction, electron hopping, and perhaps conduction in several bands.

Discussion

In the above discussion, we have found that the observed transport properties do not agree with a nominal $\text{Ba}_8\text{Cu}_{6-x}\text{Ge}_{40+x}$, $x = 0$ – 0.7 , stoichiometry. Instead, they could be explained by a single parabolic conduction band and a short mean free path. This discrepancy might arise from a narrow phase width. Stable phases might form only in the n -type regime. If the compound is assumed to be a Zintl phase, then $\text{Ba}_8\text{Cu}_{5.33}\text{Ge}_{40.67}$ is the optimum stoichiometry, which can be derived from simple electron counting with Ba, Cu, and Ge in oxidation state II, I, and IV, respectively; this is in good agreement with the 5:41 Cu:Ge composition found by Li et al.⁸ Consequently, phases can be assumed to form with a stoichiometry of $\text{Ba}_8\text{Cu}_{5.33}\text{Ge}_{40.67-v}$, where v is the vacancy concentration. For small x , a large Ge deficit results in vacancy formation, whereas for larger x , the deficit becomes smaller and consequently fewer vacancies are formed. Eventually, for the $x = 0.7$, there is a slight surplus of Ge and no vacancies are formed. A narrow phase width could thus be responsible for the vacancy formation. Vacancy formation is in accordance with the observed lattice parameters. Because of the larger covalent radius of Cu compared with Ge, a decreasing lattice parameter would be expected upon increasing x . The opposite is observed, i.e., a increases as x increases. If the sample stoichiometry is $\text{Ba}_8\text{Cu}_{5.33}\text{Ge}_{40.67-v}$, this behavior can be attributed to vacancies being occupied as x increases. The narrow range of n is another strong indication of a narrow phase width. The expected carrier concentration of 0.1 e^- to 2 holes per uc is at variance with the observed 0.05–0.2 e^- per uc. Furthermore, judging from the above figures, the electronic properties of the $x = 0.4$ – 0.7 samples are quite similar, which could be an indication that an upper substitution limit has been reached. A narrow phase width was previously suggested by Li et al.⁸ They noted a possible formation of vacancies on the $2a$ barium site and on the $6c$ and $16i$ framework sites as a result of Cu overloading. In their Zintl concept analysis, the composition was assumed to be $\text{Ba}_8\text{Cu}_{5.33}\text{Ge}_{40.67}$, with vacancies being

- (37) Bontien, A.; Pacheco, V.; Paschen, S.; Grin, Y.; Steglich, F. *Phys. Rev. B* **2005**, *71*, 165206.
 (38) Cohn, J. L.; Nolas, G. S.; Fessatidis, V.; Metcalf, T. H.; Slack, G. A. *Phys. Rev. Lett.* **1999**, *82*, 779–782.
 (39) Sales, B. C.; Chakoumakos, B. C.; Jin, R.; Thompson, J. R.; Mandrus, D. *Phys. Rev. B* **2001**, *63*, 245113.
 (40) Rodríguez-Carvajal, J. In *An Introduction to the Program FullProf 2000*; Laboratoire Leon Brillouin, CEA-CNRS: Saclay, France, 2001.

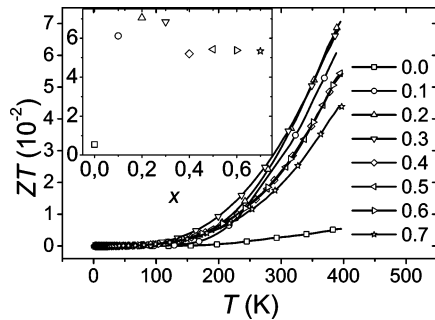


Figure 14. Thermoelectric figure of merit (ZT) as a function of temperature. The inset shows ZT at 400 K as a function of the level of substitution (x). 1/20 of the data points are shown.

formed if the molar copper content exceeded 5.33 per uc.⁸ However, the evidence for vacancies and a narrow phase width is not undisputed. The lack of any crystalline impurities other than Ge is difficult to explain if the compounds are assumed to have a narrow phase width. Copper-containing impurities would be expected, especially for small x . But no crystalline impurities are detected in the synchrotron radiation powder diffraction pattern nor in conventional XRD. The impurities might have been soluble in the ethanol employed in the sample preparation for the synchrotron diffraction experiment. Such a treatment was not employed in the conventional XRD. The expected surplus of Cu might also exist in an amorphous copper-containing phase and consequently would not be visible in diffraction experiments.

Thermoelectric Figure of Merit. The efficiency of thermoelectric energy conversion increases monotonically with the dimensionless figure of merit (ZT)

$$ZT = \frac{S^2}{\rho\kappa} T \quad (3)$$

To achieve the Carnot efficiency, ZT must be $\gg 1$. State of the art thermoelectric devices have $ZT \approx 1$. In Figure 14, the ZT values of the synthesized samples are shown. The $x = 0.2$ sample has a $ZT = 0.07$ at 400 K. But sample $x = 0.1$ is likely to out-perform it at higher temperatures because of its decreasing ρ and increasing S . Using Wiedemann–Franz’ law, we can rewrite eq 3 as

$$ZT = \frac{S^2}{L_0 + \kappa_L \rho / T} \quad (4)$$

To achieve a $ZT > 1$, S^2 must therefore be larger than the Lorentz number ($L_0 = (157 \mu\text{V K}^{-1})^2$), and the lattice thermal conductivity must be small compared to the electronic thermal conductivity. The studied samples have a relatively low lattice thermal conductivity and, depending on the doping level, a high thermopower. What impedes high ZT values is the low mobility observed in these samples, which results in a high resistivity and thereby a large $\kappa_L \rho / T$ factor. Because of their large band gaps and thermal stability, clathrates carry much interest for high-temperature energy conversion. To estimate the ZT value that can be achieved at higher temperatures, we have calculated S as a function of temperature²² for the doping corresponding to the $x = 0.1$ sample, $n = 0.04 e$. Obviously, S at high temperatures is very dependent on the band gap. In Figure 15, we show S as a

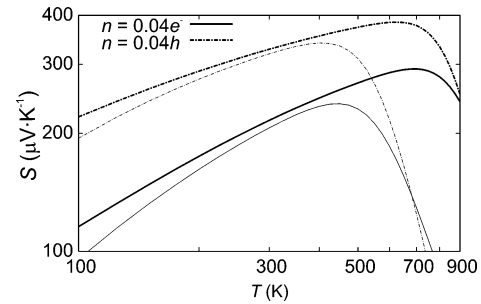


Figure 15. Calculated thermopower for $\text{Ba}_8\text{Cu}_6\text{Ge}_{40}$ with $n = \pm 0.04e$ as a function of temperature. The thin lines correspond to $E_g = 0.18$ eV (from the PBE calculation) and the thick lines to $E_g = 0.52$ eV (from the EV calculation).

function of temperature using both of the estimated gaps ($E_g = 0.18$ eV and $E_g = 0.52$ eV). Using $n = 0.04e$ we get $S = -292 \mu\text{V K}^{-1}$ at 700 K. If ρ is assumed to reach a value of $10 \text{ m}\Omega \text{ cm}$ and $\kappa = 1.8 \text{ W m}^{-1} \text{ K}^{-1}$, an estimate of ZT at 700 K would be 0.3. One further point from $g(\epsilon)$ is that the valence bands have a substantial Cu contribution near the gap, whereas the conduction bands have almost no Cu contribution near the gap. Thus, the initial purpose of the present study of investigating the influence of transition-metal d states on the transport properties could be achieved if p -doped samples could be produced. Figure 15, where S has been calculated for a $n = 0.04h$ sample, illustrates that S is indeed higher for a p -doped sample. Here, $S = 376 \mu\text{V K}^{-1}$ at 700 K is reached. Using the same parameters as above, this gives $ZT = 0.5$. Again, it should be pointed out that the low mobility due to the short mean free path limits the ZT value.

Conclusions

Eight $\text{Ba}_8\text{Cu}_{6-x}\text{Ge}_{40+x}$, $x = 0-0.7$ samples were synthesized on the basis of calculated transport properties for various shifted Fermi levels. A new synthetic route was employed and yielded single-phase samples with only minor impurities, as confirmed by powder XRD. The compacted samples were highly dense and of good mechanical strength. Changing the substitution level induced systematic changes in the electronic properties, thereby providing a handle to tune the thermoelectric properties. The observed systematic changes in the behavior of the resistivity, thermopower, and carrier concentration were compared to the transport coefficients extracted from the calculated band structure. The results agree well if the Fermi level is calculated with respect to the gap in $g(\epsilon)$ and if a short mean free path was introduced. These two observations were explained by a high concentration of vacancies, resulting in the formation of dangling bond states at the gap. The temperature dependence and magnitude of ρ , S , and n cannot be fully understood from the theoretical band structure. This is an indication that the states close to the Fermi level are localized. This results in electron mobilities that are low, but of the same order as in $(\text{Ba}/\text{Sr}/\text{Eu})_8\text{Ga}_{16}\text{Ge}_{30}$. In $\text{Ba}_8\text{Cu}_6\text{Ge}_{40}$ and similar modifications, localized states are probably due to the presence of a small amount of vacancies. In $(\text{Ba}/\text{Sr}/\text{Eu})_8\text{Ga}_{16}\text{Ge}_{30}$, the small residual resistance ratio is an indication of localized states; however, in these compounds, Ga/Ge disorder appears to

be the source of the localized states. In general, it appears as if localized states inhibit the thermoelectric performance of clathrates and further experimental and theoretical investigations are needed in order to fully explore the high-temperature thermoelectric properties of clathrates.

Acknowledgment. The synchrotron radiation experiments were performed at the Spring-8 with the approval of the Japan

Synchrotron Radiation Research Institute (JASRI) (Proposal 2005A0045ND1c-np). Dr. Eiji Nishibori and Shinobu Aoyagi are thanked for assistance during measurements. S.J. thanks the Danish Strategic Research Council for funding a stipend. G.K.H.M. thanks the Carlsberg Foundation for a grant. We are indebted to the Carlsberg Foundation and the Danish Research Councils for a Quantum Design PPMS.

CM061195Y